

INVERSION OF PHYSICALLY RECORDED ULTRASONIC WAVEFORMS USING
ADAPTIVE LEARNING NETWORK MODELS TRAINED ON THEORETICAL DATA

M. F. Whalen and A. N. Mucciardi
Adaptronics, Inc.
McLean, Virginia 22102

ABSTRACT

The objective of this work has been to demonstrate the feasibility of estimating automatically the size and orientation of subsurface defects in metals. The approach has been to (1) obtain computer-generated spectra from various elastic scattering theories, (2) use these spectra to train empirical nonlinear Adaptive Learning Network (ALN) models, and (3) evaluate the theoretically trained ALN's on eight physically recorded defect specimens via a blind test. The results demonstrate that very good defect characterization is possible and that a fully automatic and general purpose NDE system can be implemented. An average orientation error of 10.2 degrees has been achieved and the defect average volume error is 17.5 percent.

The ALN models were synthesized using theoretically generated spectral scattering data from the Born Approximation (BORN), the Extended Quasi-Static Approximation (EQSA), and the Scattering Matrix Method (SMM) digital computer programs. The type of defects simulated were oblate spheroidal voids in a Titanium alloy.

The ultimate significance of this work is to further support the mounting evidence that theoretical computer models can be used as ultrasonic calibration data in place of building physical specimens. The capability of (1) simulating many difficult-to-produce defect/geometrical reflector scenarios in various metal matrices and, (2) using the ALN methodology to develop automatic detection, characterization and sizing methods using the simulated ultrasonic echoes will yield tremendous economic benefits.

SUMMARY OF RESULTS,
CONCLUSIONS, & RECOMMENDATIONS

Results:

1. The lowest average percentage errors made in estimates of the defect size parameters "A" and "B" were 20.0 and 5.9 percent, respectively. For the orientation parameters " α " and " β ", the errors were 6.7 and 5.1 percent, respectively. The error in estimating the defect volume computed from the individual estimates of "A" and "B", was 17.5 percent. Furthermore, the three-dimensional average orientation error over the eight experiments was only 10.2 degrees. These results demonstrate the feasibility of producing an automatic flaw characterization algorithm via ALN means.
2. It was found that the long wavelength A_2 coefficient provides significant information relative to the size and orientation of spheroidal defects. For pitch-multiple-catch (PMC) data, A_2 was successfully used in conjunction with other spectral features to estimate the shorter defect radius (A) and the defect's polar angle (α). Also, a favorable comparison existed between experimental and theoretically generated PMC data. This favorable comparison could not be observed for pulse-echo (PE) data since the PE experimental data had been optimized to give maximum spectral bandwidth rather than reliable information in the low frequency (long-wavelength) regime. However, for the theoretical data, a correlation of 0.97 was found to exist between the defect's larger radius (B) and the average value of A_2 computed from the inner ring ($\theta=30^\circ$) PE transducers; also, a correlation of 0.96 existed between the defect's polar angle (α) and the ratio of inner to outer ring average value of A_2 . These results clearly demonstrate the value of A_2 as a parameter for size and orientation estimates.
3. A completely automatic and general ALN processing algorithm has been developed for defect flaw characterization which also includes a fully automatic means of computing the long wavelength A_2 coefficient. The algorithm employs deconvolution of the transducer characteristic so that the solution of problems can be achieved using any commercially available 5 MHz search unit.
4. Use of the transducer arrangement in the pulse-echo (PE) mode yielded better results than the pitch-multiple-catch (PMC) mode, at least when using ALN models trained on the BORN approximation data. This statement is supported by the fact that the average orientation error improved by 7.3 degrees when changing from a PMC to a PE transducer arrangement. Also, the total number of waveforms needed for PE array processing was a factor of 3 less than that of PMC.
5. A qualitative comparison of the PE scattering data generated by each of three theories (BORN, EQSA, and SMM) and experimental data was performed. The BORN and EQSA spectral

shapes were found to be identical for oblate spheroidal void scatterers. The only observed difference between BORN and EQSA data was that EQSA's spatial distribution of the total power feature (in the range of $0.4 < ka < 3.5$) was more closely matched to the experimental data. The spectral bandwidth (i.e., the second spectral moment) for these two theories was also in good agreement with that observed from experiment. Spectral data produced by the SMM theory possessed greater detail than that of the BORN and EQSA theories. In this respect, SMM spectra provided a closer match to experimental spectra. The SMM data was the closest of three theories to faithfully mimic the center frequency (first spectral moment) spatial distribution.

6. From a quantitative viewpoint, the three theories yielded almost identical orientation estimates, with an average error of approximately 12 degrees (over a possible 180 degrees). However, the average error in computing the defect's size varied among the three theories. For BORN, EQSA, and SMM, the average size errors were 32, 26, and 54 microns, respectively.

Conclusions

1. Use of theoretically generated data combined with ALN technology to accurately and automatically characterize spheroidal-shaped flaws via ultrasonic inspection has been favorably established.
2. The EQSA theory, compared to the BORN theory, provides a closer approximation to experimental scattering data. This is supported by the facts that (1) the EQSA-trained size models were more accurate than BORN when evaluated on experimental data; and, (2) the EQSA total power spatial distributions were in excellent agreement with the experimentally observed distributions. The EQSA program (written by J. Gubernatis) is also very efficient in generating large data bases. It is therefore recommended that other groups interested in inversion techniques consider the EQSA theory in place of the BORN theory. The SMM theory provides the closest match to experiments than the other theories investigated. However, it is believed more analysis is needed to make best use of the "more detailed" spectral information.
3. The orientation estimates for BORN PE models are superior to the BORN PMC models probably because the BORN approximation is most accurate in the backscatter position. A qualitative observation to support this fact was that the radiation pattern (or polar plot) of the scattered energy was "sharper" (i.e., more peaked) for the PE mode than in the PMC mode and matched experimental results more closely.

Recommendations

1. Improvements in estimating defect size and orientation can be achieved by (1) increasing the number of experiments in the training set from, say, 240 to about 1000; (2)

increasing the number of elements in the transmit/receive array; and (3) possibly, changing the transducer array to a more equispaced configuration.

2. The present study was concerned with evaluating three scattering theories on a common basis. In doing so, the SMM theory was considerably under-utilized because the phase information, not found in the BORN or EQSA program, was discarded from analysis for the sake of maintaining a common basis for comparison. The additional information provided by the phase spectrum should be very useful in characterizing flaws. Therefore, it is recommended that the SMM phase information be incorporated in all future work.
3. J. Rose's transformation from frequency to R-space should be incorporated into the ALN procedure to test its utility for yielding further improvements in defect characterization.
4. In the development of further flaw characterization systems, a "combined theory" data base might be considered, where the best features of each theory would be used for ALN model synthesis. In this manner, a larger and more representative feature set could possibly be postulated.
5. The present study is concerned with L→L mode scattering only; however, L→S mode scattering should also be considered in future work since the ripple period in the scattered shear wave spectrum is more observable than in the scattered longitudinal spectrum.
6. In order to realize a quantitative NDE flaw characterization system, the ability to discriminate between crack-like defects and ellipsoidal-shaped defects is necessary. A completely automatic ALN-based NDE system will need to characterize both two- and three-dimensional flaws. The present work has addressed three-dimensional defects. A similar effort should now be performed to characterize the size and orientation of two-dimensional flaws. Also, an ability to discriminate between two- and three-dimensional flaws will be needed as illustrated in Fig. 1. It is recommended that the coming year's work focus on implementing the system shown in Fig. 1.

INTRODUCTION

The determination of the characteristics of subsurface defects in materials by non-invasive techniques is an important and challenging task in the non-destructive evaluation (NDE) of materials.

The description of the scattering wave equations for defects of known geometries and material properties -- the "forward" problem -- has been a topic of several investigations. Krumhansl, Domany and Gubernatis were responsible for applying the BORN approximation to estimate the scattered power spectrum from spheroidal-shaped defects. [1]. Gubernatis later used a more powerful technique, known as the extended quasi-static approximation, to estimate scattered fields from spheroids

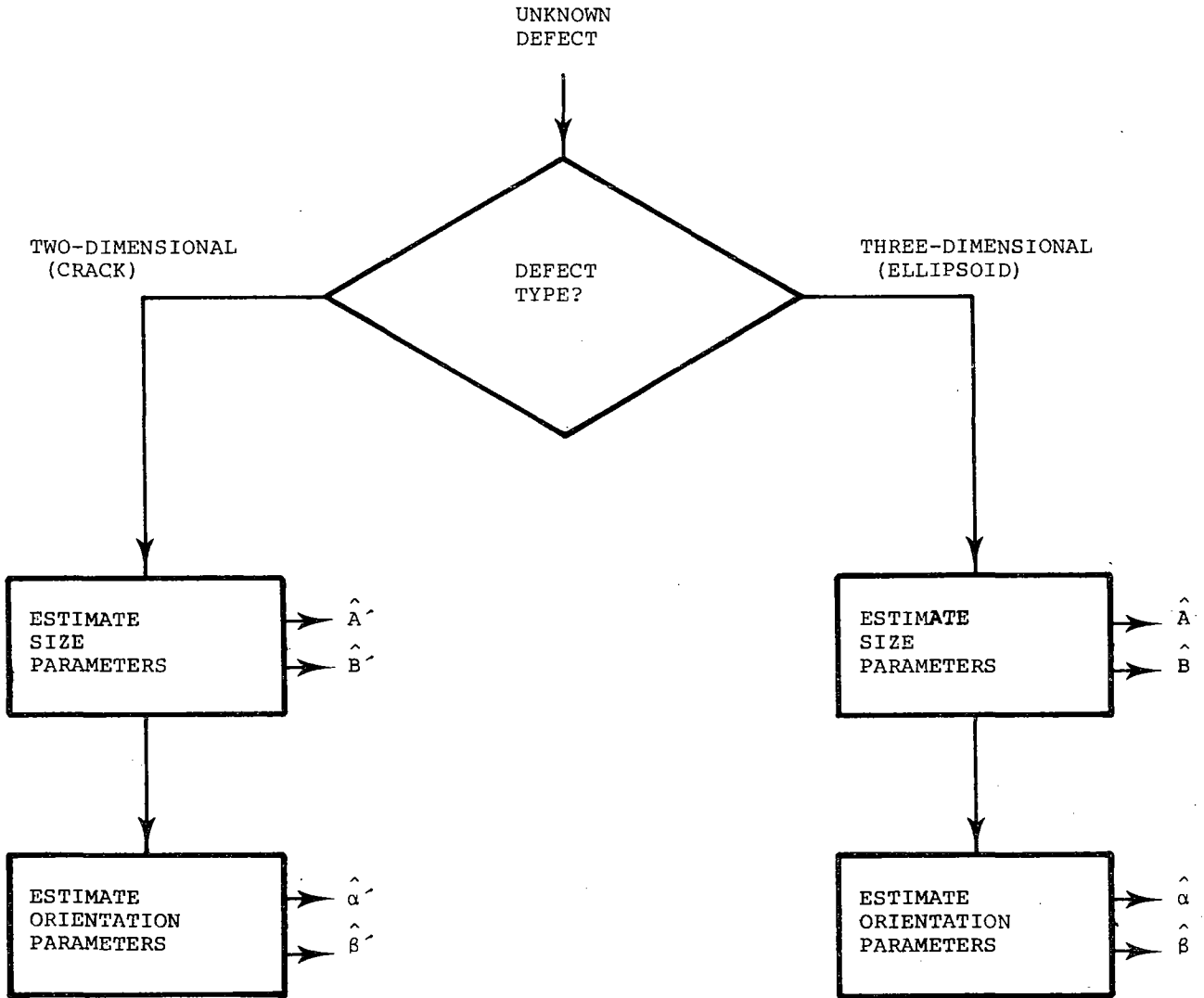


Fig. 1. Decision logic for characterizing both two and three-dimensional defects.

[2]. Rapid convergence is an advantage of both of these methods. Varadan and Poa introduced a matrix approach to elastic wave scattering applicable to arbitrarily shaped scatterers [3]. The computer implementation of this technique requires considerably more computation than the aforementioned approximation, but the solutions are more accurate. Additionally, both amplitude and phase information are yielded from the SMM solution. Achenbach has developed and programmed the equations of scattering from elliptical cracks based on elastodynamic ray theory [4].

From the NDE standpoint, the interest has been in the solution of the "inverse" problem; namely, how can the defect characteristics be described knowing the theoretical, or observed, scattering waveform. Studies by Tittmann and Cohen have shown some success using the BORN approximation [5]. Richardson has been successful with an inversion procedure utilizing measurements in the long wavelength Rayleigh regime [6]. Rose has shown that the effective radius of a defect can be estimated by applying sine transforms to the scattered amplitude spectra [7].

Mucciardi, Whalen and Shankar were the first to apply a systematic and automatic signal processing approach -- Adaptive Learning Network methodology -- to the inverse problem [12]. This report presents results of this continuing study in which characteristics of spheroidal defects, imbedded in a Ti-64 alloy, were measured accurately by analysis of the ultrasonic energy scattered from these defects.

DEFECT GEOMETRY, DATA BASE, AND ARRAY CONFIGURATION

The defect geometry, theoretical data base characteristics, the transducer array geometry, and the experimental data set are described in this section. The present work has been confined to oblate spheroidal voids.

Defect Geometry

A spheroid is a three-dimensional surface formed by rotating an ellipse about one of its axes. When the rotation is about the minor axis, the result is an oblate spheroid. The spheroid's size and orientation can be specified uniquely by four parameters (labelled A, B, α , and β) as illustrated in Fig. 2. The following definitions apply:

- A - minor radius (along one dimension)
- B - major radius (along two dimensions)
- α - polar orientation: angle between positive Z-axis and the symmetry axis
- β - azimuthal orientation: angle between positive X-axis and projection of the symmetry axis on the X-Y plane

Throughout the remainder of the report, the defect's geometry will be represented by these four parameters. Also, the ALN models are synthesized to directly estimate these four parameters. The spheroid's volume is defined as $(4\pi/3)AB^2$.

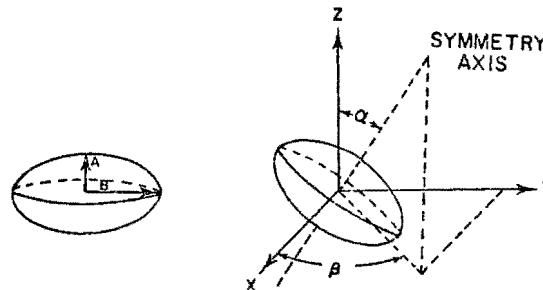


Fig. 2. Oblate spheroid coordinate geometry.

Theoretical Data Base

Identical training data bases were generated from each of the three computerized spheroid scattering theories (BORN, EQSA, and SMM). A total of 240 synthetic experiments were produced in each case. An "experiment" consisted of generating the scattered power spectrum of a differential cross-section at 17 fixed positions in space for a given defect size and orientation. Six sizes, each at 40 orientations, were represented as shown in Table 1. The $ka^{1/3}$ range of the theoretical data was 0.297 to 4.361. So, information in both the long and medium wavelength regimes was represented.

In the computer programs, the elastic constants of the Ti-64 host material were set to:

$$\begin{aligned}\lambda &= .965 \times 10 \text{ dynes/cm} \\ \mu &= .406 \times 10 \text{ dynes/cm} \\ \rho &= 4.42 \text{ gm/cm}^3\end{aligned}$$

where λ and μ are the Lamé parameters and ρ is the material density.

The longitudinal and shear wave velocities in the medium are determined from these values. The elastic constants of a void are all equal to zero.

Only L→L mode scattering was considered. (The shear wave spectrum should be considered in future work since the period of the spectrum is about one-half that of the longitudinal spectrum. This is an important consideration in physical band-limited systems since the ripple period contains information relative to the physical characteristics of the defect.)

Transducer Array Geometry

Both pitch-multiple-catch (PMC) and pulse-echo (PE) transmitter/receiver arrays were used to measure the scattered spectrum. Theoretical PMC data were generated only for the BORN program due to cost considerations. PE data were generated from each of the three scattering theories. The 17 transducer positions were fixed to cover a 120-degree solid angle aperture on the surface of

$1/\lambda$ "ka" is the product of the wave number $(\frac{2\pi}{\lambda})$, λ = wavelength) and the defect radius. If $ka < 1$, the wavelength is larger than the defect radius.

Table 1. Spheroidal defect sizes and orientations represented by the theoretically-generated power spectra. Scattering data at 40 orientations were produced for each defect size.

SIZE NUMBER	DEFECT SIZE		ka RANGE	
	A (MICRONS)	B (MICRONS)	MIN.	MAX.
1	50	300	0.297	2.616
2	150	300	0.297	2.616
3	100	400	0.396	3.488
4	200	400	0.396	3.488
5	100	500	0.496	4.361
6	300	500	0.496	4.361

6 SIZES

ORIENTATION NUMBER	DEFECT ORIENTATION	
	α (DEGREES)	β (DEGREES)
1	1	65
2	10	
3	20	
4	30	
5	40	
6	50	
7	60	
8	70	
9	80	
10	89	65
11	1	150
↓	↓	↓
20	89	150
21	1	235
↓	↓	↓
30	89	235
31	1	320
↓	↓	↓
40	89	320

40 ORIENTATIONS

in incremental steps of .39 MHz. Hence, each waveform contained 21 points. Only the received longitudinal waves considered in this study (to conform to the available experimental data which were only recorded in the L-L mode).

In the pulse-echo mode, each of the 17 transducers were used in the backscatterer mode only. Therefore, only 17 waveforms were processed in each experiment, compared to the 48 in the PMC mode. The PE array configuration is shown in Fig. 4.

Experimental Data Base

The eight physical defect specimens were fabricated by the Rockwell Science Center; the construction process and the data collection can be found in Reference [5]. The size and orientation parameters of the defects are listed in Table 2.

Table 2. Size and orientation parameters of the eight physically recorded spheroidal defect specimens

EXPERIMENT NUMBER	DEFECT SIZE		DEFECT ORIENTATION	
	A (MICRONS)	B (MICRONS)	α (DEGREES)	β (DEGREES)
1	200	400	0	0
2	200	400	30	225
3	100	400	80	160
4	100	400	0	0
5	200	400	80	160
6	100	400	30	180
7	200	400	30	180
8	100	400	30	225

WAVEFORM PROCESSING: DECONVOLUTION & FEATURE EXTRACTION

Overview

The general processing strategy of the spheroidal flaw characterization algorithm is diagrammed in Fig. 5. A set of "primary" and "secondary" features were computed from the extensive set of "experiments" generated from each of the scattering theory programs. The primary features were selected to measure global characteristics of the scattered spectra; the secondary features were spatial combinations of the primary features. The secondary features were used as inputs to train four ALN models to estimate the defect's size and orientation parameters, respectively. These models were evaluated subsequently via a blind test on physically recorded defect specimens processed in a manner compatible with the theoretical data, as shown in Fig. 5.

Primary Spectral Features

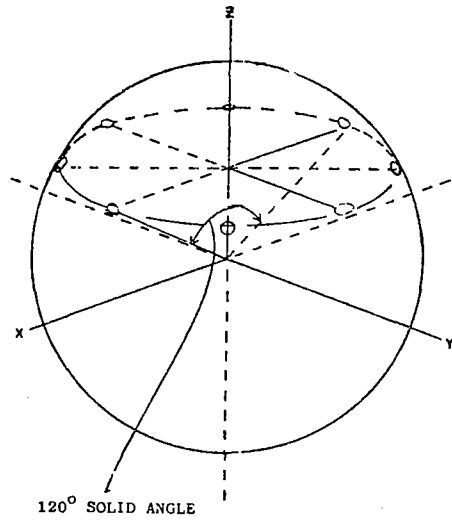
The primary feature computation was identical for both PMC and PE experiments. Fig. 6 shows the basic steps for computing primary features from the ultrasonic experimental data. Each scattered experimental UT waveform was digitized at 100 MHz and a block of 250 samples was the time window of interest. The time domain waveforms $X(t)$

a spherical "part". Hence, 33 percent of the total surface area was covered.

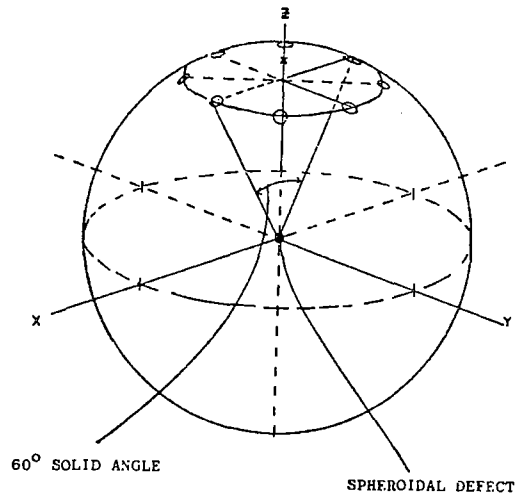
The transducer arrangements for the PMC mode are shown in Fig. 3.

The transducer configuration consisted of two circular arrays of eight elements each, and a top center (a north pole) transducer. The "inner ring" array covered a 60-degree solid angle surface, and the "outer ring" a 120-degree solid angle surface. The "north pole" transducer plus four transducers in the outer ring were used to transmit a longitudinal wave. Both inner and outer rings were used as receivers for the north pole transmitter, but only the inner ring receivers were used when transmission was initiated at any of the four outer ring transmitters. Hence, no PE information was used in the PMC mode. A total of 48 waveforms per experiment was generated in this manner.

The theoretical spectral bandwidth was chosen, for each waveform, to lie between 1.0 and 8.8 MHz



OUTER RING RECEIVERS



INNER RING RECEIVERS

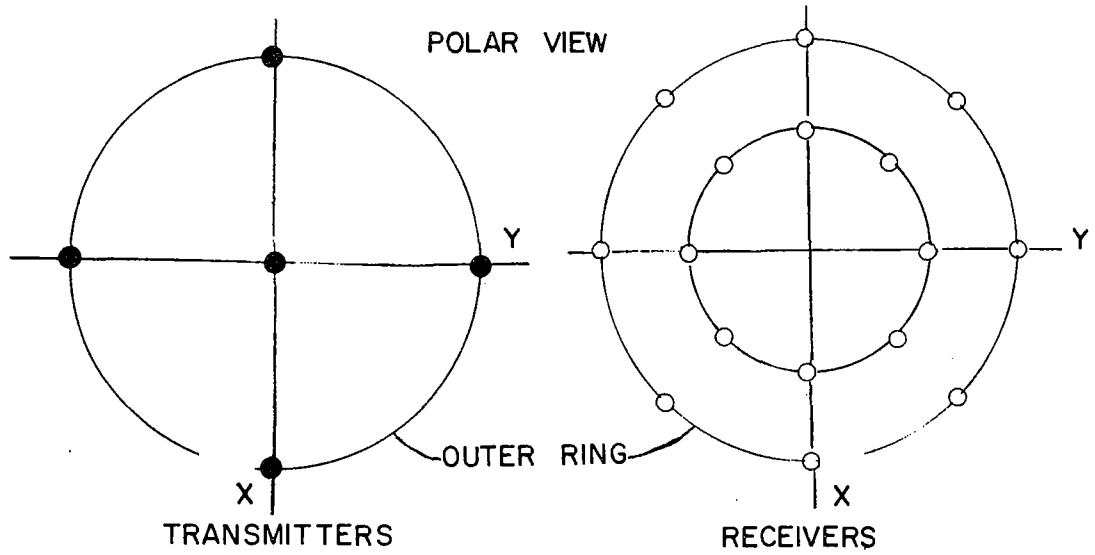
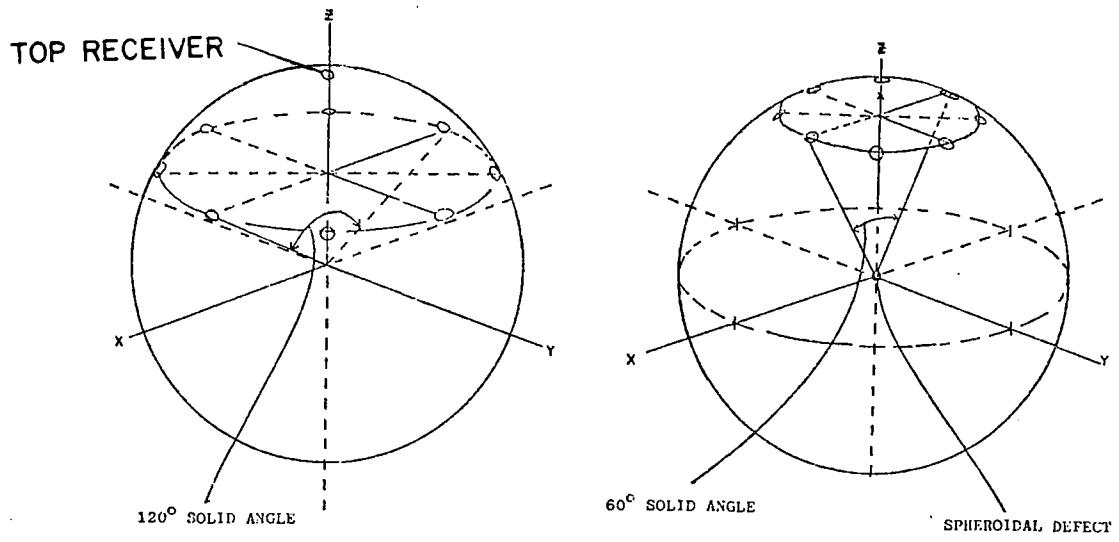
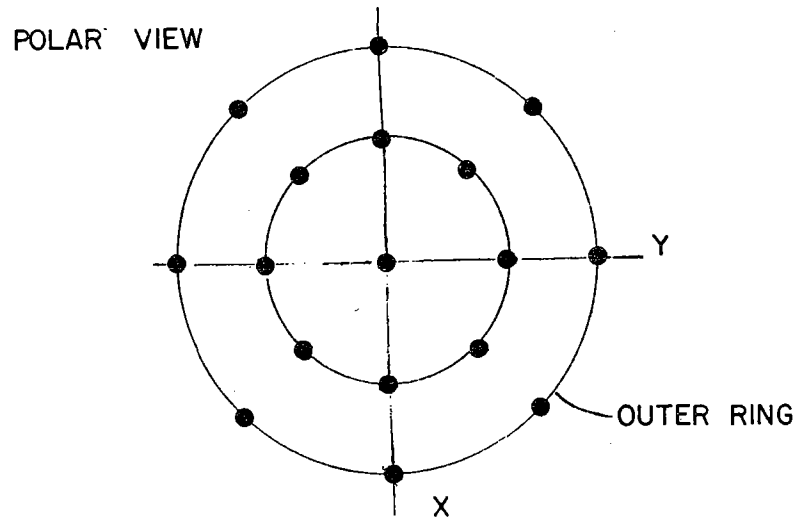


Fig. 3. Pitch-catch transmitter and receiver positional configuration



OUTER RING RECEIVERS

INNER RING RECEIVERS



TRANSMITTER / RECEIVERS

Fig. 4. Pulse-echo transmitter and receiver positional configuration.

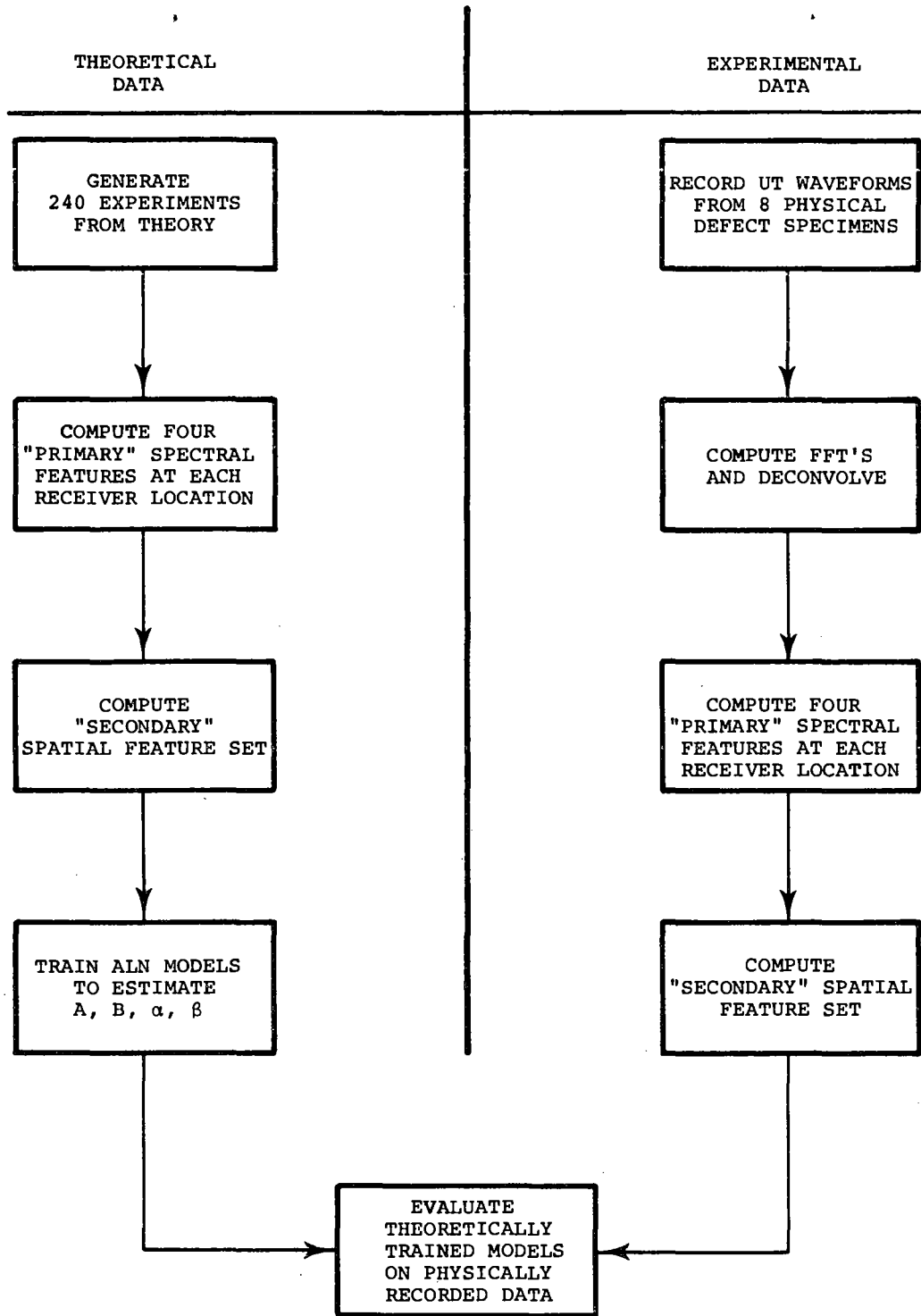


Fig. 5. Processing strategy for spheroidal flaw characterization algorithm

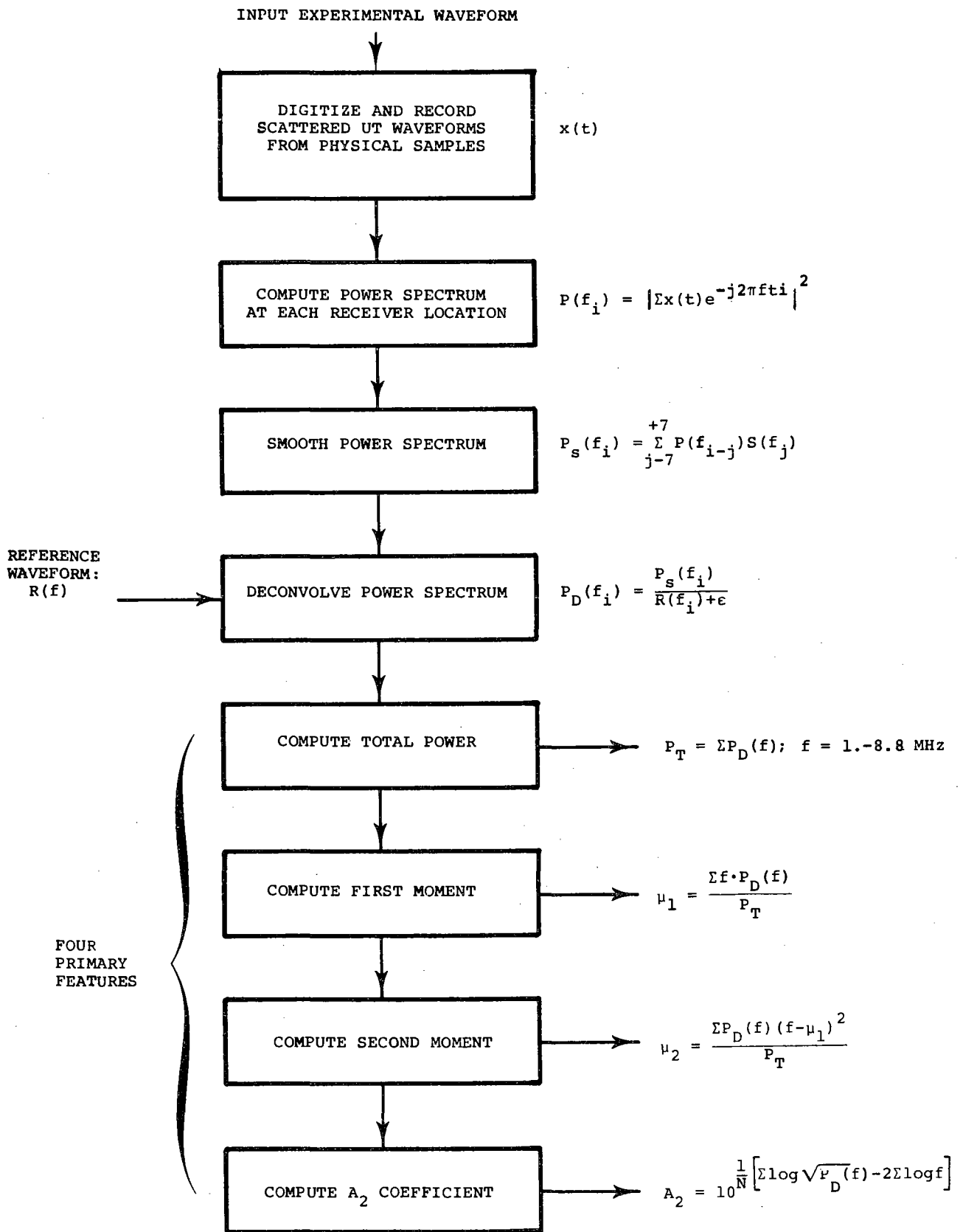


Fig. 6. Flow chart showing primary feature computation for both PMC and PE experimental data

were padded with zeros to 1024 samples and transformed to the frequency domain via the Fast Fourier Transform. A 512-point power spectrum ($P(f)$) was computed, having a maximum frequency of 50 MHz. The frequency resolution was 0.09766 MHz. The last 412 points in the spectra were discarded since they were well outside the 1-8 MHz transducer bandwidth. Visual examination of the power spectra showed considerable low frequency energy in the 0.1- to 0.9-MHz band, which was below the response of the transducer. (This artifactual information was probably caused by the recording instrumentation.) The spectral components in this low frequency band were set to zero as a means of removing the unwanted low frequency information.

Another somewhat undesirable characteristic was the presence of jagged ripples "riding" on the spectral envelope. These could have been side lobes caused by FFT processing or information pertaining to the defect itself. To de-emphasize their presence, a 15-point symmetric smoothing filter was convolved with each spectrum to low-pass-filter the spectral ripples. This operation was performed as follows:

$$P(f_i) = \sum_{j=-7}^{+7} P(f_{i+j}) S(f_j); \quad i = 1, 93 \quad (1)$$

where

$P_S(f_i)$ = the i -th smoothed spectral point,
 $P(f_i)$ = the i -th unsmoothed spectral point,
 $S(f_i)$ = the symmetric smoothing filter.

The filter function $S(f)$ was Spencer's smoothing formula. A list of the coefficients and the transform characteristics can be found in Reference [8]. An equivalent effect to smoothing could also be obtained by implementing a multiplication window on the time domain echo responses such as the Hamming or Kaiser-Bessel windows.

Deconvolution

In order to desensitize the algorithm to the specific effects of the transducer and pulser/receiver, a deconvolution process was employed. In addition to being desirable from the point of view of creating a more general algorithm, deconvolution was necessary to accurately compute the long wavelength A_2 coefficient. The deconvolution operation was performed by dividing the power spectra of the scattered waveforms by the sum of the power spectra of a reference waveform and a stabilizing constant, as represented by the equation:

$$P_D(f_i) = \frac{P_S(f_i)}{R(f_i) + \epsilon} \quad (2)$$

where

$P_D(f_i)$ = the discrete deconvolved spectrum,
 $P_S(f_i)$ = the smoothed spectrum,
 $R(f_i)$ = reference spectrum,
 ϵ = constant computed from the noise level and desired bandwidth of the deconvolved signal.

The reference spectrum, $R(f_i)$, was the power spectrum of the through-wall pitch-catch echo response in a T_1 sample when no defect was present. The quantity, ϵ , in (2) is added to each value of

$R(f_i)$ to inhibit deconvolution instability at the tail ends of the transducer bandwidth. A suitable choice for ϵ was found to be 10 percent of the peak value of the reference spectrum. Additional information regarding deconvolution can be found in References [9], [10] and [11].

The total power feature, P_T , was computed by summing the power spectral values over the approximate range of 1.0-8.8 MHz. This was the full usable portion of the deconvolved spectrum. This spectral feature has been established previously as informative relative to the defect size and orientation when comparing BORN-generated data to physical data [12]. The total power feature was computed as follows:

$$\text{total power: } T_P = \sum_{f_i = 1.0-8.8 \text{ MHz}} P_D(f_i); \quad (3)$$

The first and second spectral moments were included as primary spectral features in order to: (1) monitor spectral shifts and changes in bandwidth relative to different receiver spatial locations and different sized and oriented defects in the experimental data and, (2) compare these spectral changes to those observed in the theoretical data. The formulas for computing these features are:

$$\text{first moment: } \mu_1 = \left(\frac{1}{T_P} \right) \sum_{f_i = 1.0-8.8 \text{ MHz}} P_D(f_i) f_i; \quad (4)$$

$$\text{second moment: } \mu_2 = \left(\frac{1}{T_P} \right) \sum_{f_i = 1.0-8.8 \text{ MHz}} P_D(f_i) (f_i - \mu_1)^2; \quad (5)$$

One convenient aspect of the spectral moments is that they are self-normalizing with respect to signal amplitude, hence the theoretical and experimental values can be compared directly.

Long Wavelength Feature (A_2) Computation

Inclusion of the long wavelength A_2 coefficient as a primary spectral feature was motivated by Richardson's favorable comparison of theoretical to experimental results for this parameter [6]. Considerable analysis of scattering theory in the long wavelength regime has been performed by Rice [13]. The goal of the work presented here was to develop an automatic means for determining A_2 , the coefficient of the first term in an even power series expansion of the scattered magnitude spectrum. In order to eliminate the need for establishing a constant of proportionality between the theoretical and experimental results, each spectrum was normalized by dividing each component by the total power feature before computing A_2 .

The log-log magnitude spectrum was formed from the power spectrum over the range of 1.0 to approximately 2.5 MHz. This corresponded to k_a values in the range of 0.4-1.2 for defects of 400 μm radius. Now, $\log A_2$ can be found by computing the log-power axis intercept from the linear portion of the log-log spectrum having a slope of two. A_2 can then be found by exponentiation. The slope-of-two portion of the power curve was not known and, hence, had to be located by computing 120 linear regression coefficients over the above-mentioned range and then determine which contiguous group of points in the log-log spectrum came closest to having a slope of two. The intercept was then

formed by the extrapolation formula:

$$\text{intercept: } \log A_2 = \frac{1}{N} \sum_{j=1}^N Y_j - \frac{2}{N} \sum_{j=1}^N X_j \quad (6)$$

where, X and Y are the logarithmic spectral values f_j and $P_y(f_j)$ over the best fitting slope-of-two range. A flow chart showing computation of A_2 is shown in Fig. 7.

The primary features were computed from the theoretical data bases in the same manner as mentioned above, with the exception of the steps involving power spectral computation, spectral smoothing, and deconvolution.

Computation of the primary features represented a considerable reduction in the amount of data associated with each experiment. Instead of storing a scattered waveform at each receiver location, only four representative values need be saved.

Secondary Spectral Features

The "secondary" features were statistical quantities computed mainly from the circular receiver arrays. Their purpose was to quantify the spatial distribution of the primary features. The number and type of features varied slightly between the PMC and PE experiments due to the greater number of receivers for PMN. Also, the total power of the BORN PMC data was normalized around each receiver ring instead of a single constant for all total power in the experiment. It had been noted that in last year's effort [12], the power distribution in the polar direction was significantly greater from the BORN program than that observed in the experimental data.

Secondary Spectral Features: Pitch-Multiple-Catch Mode

Four general types of PMC secondary features were computed:

1. Statistical: sample means and standard deviations;
2. Circular: circular mean and circular variance;
3. Ratios of primary features;
4. Eigenvalues of correlation matrix.

The statistical features were averages and standard deviations of the primary features around the inner and outer receiver arrays. The mean values for the total power primary features were not included since they were normalized as mentioned above.

The circular mean was an angular feature which located the first moment of the scattered power around a circular receiver array. This feature was thought to be useful in determining β , the azimuthal defect orientation angle. Calculation of the CM was as follows:

$$CM = \tan^{-1} (S/C) + \gamma$$

where:

$$S = \sum_{\phi=0}^{315^\circ} P(\phi, \theta) \sin \phi$$

$$C = \sum_{\phi=0}^{315^\circ} P(\phi, \theta) \cos \phi$$

and

$$\gamma = 0 \text{ if } S > 0, C > 0$$

$$= \pi \text{ if } C < 0$$

$$= 2\pi \text{ if } S < 0, C > 0$$

$P(\phi, \theta)$ = one of the primary features at receiver position (ϕ, θ)

S and C were also used as secondary features. In the above computation, θ remained fixed at either 30 degrees (inner ring) or 60 degrees (outer ring); therefore, eight terms were summed in computing either S or C.

The circular variance feature is defined between zero and unity and was a measure of the power dispersion about the circular mean of a given circular array:

$$CVAR = 1 - \sum_{\phi=0}^{315^\circ} P(\phi, \theta) \cos(\phi - CM)$$

For each of the four outer ring ($\theta=60$ degrees) transmitters, a ratio feature RI was computed, defined as follows:

$$RI(\phi) = \frac{[P(\phi-45, 30) + P(\phi-90, 30) + P(\phi-135, 30)]}{[P(\phi+45, 30) + P(\phi+90, 30) + P(\phi+135, 30)]}$$

A four-by-four correlation matrix was computed by correlating the primary features distributions at the inner ring receivers for each pair of the four outer ring transmitters. For instance, the correlation coefficient, $\rho_{i,j}$, for transmitters i and j can be computed as follows:

$$\rho_{i,j} = \frac{\sum_{\phi=0}^{315^\circ} [P_i(\phi, 30) - \bar{P}(30)] [P_j(\phi, 30) - \bar{P}(30)]}{\sigma_{P_i} \sigma_{P_j}}$$

where,

$$i = 1, 2, 3, 4; \quad j = 1, 2, 3, 4$$

The eigenvalues of the $\rho_{i,j}$ matrix were used as features.

As mentioned above, the standard deviations (σ) around the 8-element arrays were computed. For each of four outer transmitters, one such σ was computed. The mean and standard deviation of these four σ 's were also used as features.

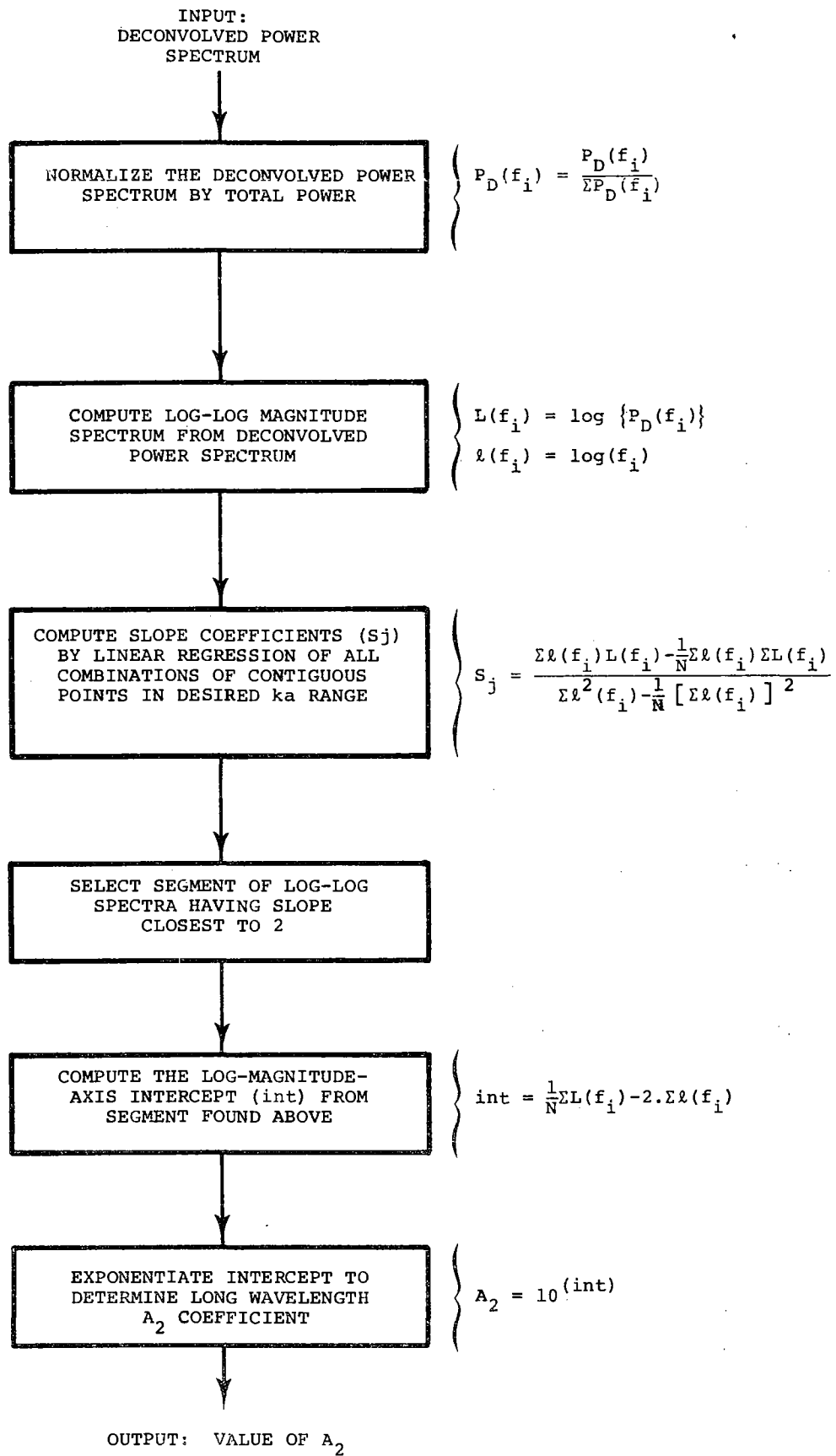


Fig. 7. Flow chart to compute long wavelength A₂ coefficient

Secondary Spectral Features: Pulse-Echo Mode

The PE total power at each receiver was normalized by the sum of the total power of all 17 receivers. In this manner, the three-dimensional relative scattered power distribution was not destroyed. There were five types of features computed from the PE primary features:

1. Statistical;
2. Circular;
3. Ratios;
4. Eigenvalues;
5. β -plane features.

The statistical features were the sample mean and variance of the primary features computed from the inner and outer receiver rings. The circular means and variance were also computed around these rings, in the same manner described above. The ratio features were the mean inner ring primary features divided by the mean outer ring primary features.

The eigenvalue features for the PE data were different from those described above in the following way. A spatial covariance matrix was computed, weighted by the values of the primary features. For instance, using the total power (P_i) as the weighting coefficient, the spatial covariance matrix was computed as:

$$\bar{C} = \begin{bmatrix} 17 & & & \\ \sum_i P_i X_i^2 & \sum P_i X_i Y_i & \sum P_i X_i Z_i & \\ \sum P_i X_i Y_i & \sum P_i Y_i^2 & \sum P_i Y_i Z_i & \\ \sum P_i X_i Z_i & \sum P_i Y_i Z_i & \sum P_i Z_i^2 & \end{bmatrix}$$

The three eigenvalues of this matrix yield information about the spatial distribution of total power (P_i), which, in turn, yields information about the defect's orientation and size. An explanation of the meaning of these eigenvalues can be found in Reference [14].

Another type of secondary feature was computed from five receivers in the β -plane. An estimate for the defect azimuthal angle " β " was computed from the circular mean of the inner and outer rings. If the estimated value of β -- denoted as $\hat{\beta}$ -- fell along an increment of 45 degrees, five receivers were found at 30-degree increments in that plane. If $\hat{\beta}$ fell at an arbitrary position, the values at these missing receiver positions were estimated by interpolation. From these five receivers, the mean, standard deviation, first and second moments, and ratio of three inner to four outer values were taken. There were 52 secondary PE features computed.

RESULTS

The most significant aspect of this work was to establish that the theoretically trained ALN models yielded accurate size and orientation estimates when evaluated on eight physically recorded spheroid samples via a blind test. These numerical estimates are presented below. It was also interesting to note that the ALN modeling procedure recognized different spectral feature sets for each

of the different theories, which suggests that even better performance might be obtained by synthesizing models on a combined theory feature set. This is recommended for future work. It should be noted that the evaluation was "blind" in the sense that no portion of the physical data was used to influence the ALN model synthesis procedure.

Qualitative comparisons of the theoretical and experimental data are presented below in the form of radiation patterns (polar plots) of the primary features. Also, a comparison of the scattered spectra for the three theories is shown. The BORN and EQSA spectra were identical in their overall shape (i.e., smooth and sinusoidal in nature), while the SMM-generated spectra possessed greater spectral detail. The SMM spectral most closely matched the experimental data.

The numerical estimates for the physical defect parameters A, B, α , and β for each of the eight experiments are presented in Table 3. Also listed are the estimated volume (V), computed from the ALN outputs for A and B; and the "orientation error", computed from the ALN estimates for α and β . Four methods were used in estimating each parameter as shown. The average absolute error (AAE) and the percentage average absolute error (%AAE) were computed on all estimates over the eight experiments and appear in the right-hand columns^{2/}. The "true" experimental values for A, B, α , β , and V are shown in the top row of each group.

Estimates for the size parameters "A" and "B" were comparable for each of the four methods. The lowest percentage average absolute errors for these parameters were 20.0 percent for "A", yielded by the EQSA PE model, and 5.9 percent for "B", yielded by the BORN PE model. Note, however, that the average absolute errors are about the same for these two models (about 25 microns). Also, note that each of the three theories yielded approximately the same results.

Figure 8 is a pictorial display of the size estimates presented in Table 3. Here, ellipses are drawn whose major and minor axes are the model estimates for A and B for each of the four methods. The true estimates are shown at the top of the figure.

Estimates for the polar orientation " α " were definitely superior in the PE models compared to those produced by the BORN PMC model. Improvements of approximately 12 percent were observed for the former methods. The probable reason for increased performance was due to reliable generation of theoretical "backscatter" data. The BORN program's ability to generate pitch-catch data is suboptimal. Pitch-catch data from the theories other than BORN were not pursued because of cost considerations in generating the computer data.

^{2/}%AAE for A and B was computed by dividing the absolute difference between true and estimated values by the true value, then averaging over eight experiments. The %AAE and α and β was computed by dividing the AAE for these values by their respective ranges, 90 and 180.

Table 3. Size and orientation estimates for the eight experimental spheroidal defect samples determined from the theoretically-trained ALN models.

PARAMETER TYPE	METHOD	EXPERIMENT NUMBER								ERROR	
		1	2	3	4	5	6	7	8	AAE	%AAE
MINOR AXIS A (MICRONS)	TRUE 'A'	200	200	100	100	200	100	200	100	--	--
	BORN PMC	207	250	88	73	433	106	226	96	45.6	25.9
	BORN PE	198	189	178	101	191	201	195	175	35.3	33.6
	EQSA PE	209	174	129	149	194	135	157	95	25.3	20.0
	SMM PE	186	147	259	121	175	145	147	64	50.7	41.7
MAJOR AXIS B (MICRONS)	TRUE 'B'	400	400	400	400	400	400	400	400	--	--
	BORN PMC	442	412	424	419	426	421	481	394	28.9	7.2
	BORN PE	474	417	365	428	385	397	399	417	23.8	5.9
	EQSA PE	383	364	379	361	434	371	379	389	26.0	6.5
	SMM PE	278	342	285	458	395	410	354	444	57.3	14.3
POLAR ANGLE α (DEGREES)	TRUE ' α '	0	30	80	0	80	30	30	30	--	--
	BORN PMC	10	13	80	23	38	31	6	2	18.1	20.1
	BORN PE	14	18	76	8	63	34	41	38	9.8	10.3
	EQSA PE	4	28	80	11	67	42	53	36	8.9	9.9
	SMM PE	7	14	80	-5.9	83	24	40	29	6.0	6.7
AZIMUTHAL ANGLE β (DEGREES)	TRUE ' β '	--	225	160	--	160	180	180	225	--	--
	BORN PMC	--	225	166	--	209	180	180	225	9.2	5.1
	BORN PE	--	207	158	--	189	200	199	217	16.0	8.9
	EQSA PE	--	198	160	--	183	195	192	209	15.5	8.6
	SMM PE	--	223	169	--	183	188	188	232	9.5	5.3
VOLUME ^{1/} V (MICRONS ³ x 10 ⁶)	TRUE 'V'	134	134	67	67	134	67	134	67	--	--
	BORN PMC	169	179	66	54	329	79	219	62	48.9	39.4
	BORN PE	186	138	99	77	119	133	130	127	30.4	38.3
	EQSA PE	128	97	78	81	153	78	94	60	18.1	17.5
	SMM PE	60	72	88	119	114	102	77	53	41.9	42.6
ORIENTATION ERROR ^{2/} 'OE' (DEGREES)	BORN PMC	10.0	17.0	5.9	23.0	57.7	1.5	23.9	28.0	20.9	11.6
	BORN PE	14.0	14.0	4.5	8.0	32.2	11.4	15.5	8.9	13.6	7.5
	EQSA PE	4.0	13.1	0.0	11.0	25.6	14.9	24.2	10.4	12.9	7.2
	SMM PE	7.0	16.0	8.9	4.9	22.9	7.0	11.0	3.6	10.2	5.6

$$\frac{1}{V} = AB^2 (4\pi/3) \times 10^{-6}$$

$$\frac{2}{OE} = \cos^{-1} [x\hat{x} + y\hat{y} + z\hat{z}]$$



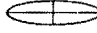
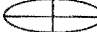
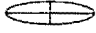
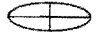

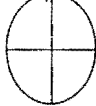

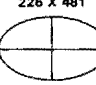

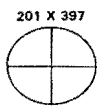


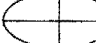
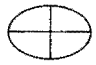
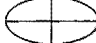
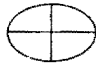






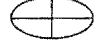









TRUE ESTIMATED	 100 X 400	 200 X 400
BORN PMC	88 X 424  106 X 421 	73 X 419  96 X 394  207 X 442  433 X 426  250 X 412  226 X 481 
BORN PE	178 X 365  201 X 397 	101 X 428  175 X 417  198 X 474  191 X 385  189 X 417  195 X 399 
EQSA PE	129 X 379  135 X 371 	149 X 361  95 X 389  209 X 383  194 X 434  174 X 364  157 X 379 
SMM PE	259 X 285  145 X 410 	121 X 458  64 X 444  186 X 278  175 X 395  147 X 342  147 X 354 

Fig. 8. True versus estimated sizes for eight experimentally recorded oblate spheroid defects.

Four methods were used to train ALN's: 1) BORN pitch-multiple catch; 2) BORN pulse echo; 3) Extended Quasi-Static Approximation (EQSA) pulse echo; and 4) the Scattering Matrix Method (SMM) pulse echo. The "true" sizes were 100 x 400 microns and 200 x 400 microns, each at four orientations.

The smallest observed average absolute error for the orientation estimates were 6.0 degrees for the polar angle "α", yielded by the SMM PE model, and 9.2 degrees for the azimuthal angle "β", yielded by the BORN PMC model. Both values are excellent error estimates for the defect orientation considering the sparse spatial separation of the transducers: 30 degrees in the polar direction and 45 degrees in the azimuthal direction. One way that the orientation accuracy could be improved is by increasing the number of array elements.

Estimates of the spheroid's volume (\hat{V}) were computed from the individual A and B estimates for each of the four methods by the formula:

$$\hat{V} = (4\pi/3)\hat{A}\hat{B}^2$$

The results are listed in Table 3. The EQSA PE models provided the best estimates of volume with a 17.5 percent average absolute error.

Another way of presenting the orientation error is by measuring the absolute angle between the true symmetry axis (S) and the estimated symmetry axis (\hat{S}). This is computed from the definition of the inner product of the two orientation vectors:

$$S \cdot \hat{S} = |S| |\hat{S}| \cos \psi = S_x \hat{S}_x + S_y \hat{S}_y + S_z \hat{S}_z$$

If the magnitudes of S and \hat{S} are arbitrarily set to unity:

$$\psi = \cos^{-1} (S_x \hat{S}_x + S_y \hat{S}_y + S_z \hat{S}_z)$$

where the X, Y, and Z components of S and \hat{S} are computed from the true and estimated orientation angles, α and β. Table 3 shows the smallest average absolute orientation error to be 10.2 degrees for the SMM PE models. A way of viewing the orientation error is shown in Fig. 9. Each axis represents zero orientation error for each of the four methods. The smaller arrows on the outside of the circle represent the computed errors for each of the eight experiments. (The error will never be negative, by definition.) Note that each of the three theories produced comparable results in the PE mode.

A list of the features selected by each of the four methods is given in Table 4. From left to right, the columns in each group refer to the primary feature type, the receiver group from which the secondary feature was computed, a description of the secondary feature, and the ALN models which selected that feature as being important. Note that the selected BORN PMC feature set was considerably larger than those selected by the other methods. This was due to the more extensive candidate features list accommodating the larger number of PMC receivers.

The ALN model based on EQSA PE selected a total power feature almost exclusively, whereas the other methods utilize more of the spectral features.

Radiation plots of the four primary features for a 200 μm by 400 μm oblate spheroid defect with orientation α = 80 degrees and β = 160 degrees are shown in Fig. 10. In each plot, the magnitude of the primary feature at each inner ring receiver

was plotted as a function of the azimuthal receiver angle φ. Both theoretical and experimental data are superimposed on each plot. Notice the similarity between all three theories and experiments for the total power feature. Also, it can be seen how dissimilar the A₂ coefficients are when comparing theory and experiment. As mentioned previously, one reason for this is that the PE experimental data were recorded with the pulser set to provide the broadest band response. This yielded very few data points in the ka < 0.5 region; hence, the values of A₂ for the experimental data were greatly distorted. (But, as discussed above, the A₂ parameter was found to be very informative with respect to the theoretical data. Therefore, one of the recommendations is to rerecord data with better low frequency content.)

COMPARISON OF THEORETICAL AND EXPERIMENTAL SPECTRA

A comparison of the theoretical (SMM) and experimental power spectra is shown in Fig. 11. The data used in generating these plots were the pulse-echo data described in Section 3 of this report. Each plot was normalized by its peak value; hence, the largest value in each plot is unity. The left-hand plots -- Fig. 11 (a, b, and c) -- are from the 100 μm by 400 μm defect at polar orientations of 30, 60, and 90 degrees, respectively. The right-hand plots -- Fig. 11 (c, d, and e) -- are from the 200 μm by 400 μm defect at the same three orientations. Note that Fig. 11 (a and b) have favorable comparisons over the entire frequency range of 1.0 to 8.8 MHz. Fig. 11 (d) compares quite well up to 7.0 MHz. The remaining figures are slightly stretched in the mid-frequency range, but the general shapes of the theoretical and experimental curves are the same. Also, note that all six plots compare favorably in the long wavelength (low frequency) regime.

Unfortunately, there was much variation in the experimental data. Low signal-to-noise ratio caused the defect's impulse response to be unrecognizable in about 30 percent of the experimental data.

The major reasons for differences between the theoretical and experimental data are: (1) limited transducer bandwidth at the low and high frequencies; (2) error in experimental measurements; and (3) possible divergence in the theory at high frequencies.

The plots in Fig. 11 show that marginal information relative to the shorter defect size parameter "A" is contributed by the spectral moment primary features. Note that there is very little shift in the major peaks between the 100 μm by 400 μm plots and the 200 μm by 400 μm plots. However, it does appear that plots having the larger "A" dimension also have a greater "ripple" in their spectra. This ripple could be quantified by performing a cepstrum transformation on the defect's time domain impulse response. Another method of quantifying this ripple is by application of J. Rose's sine transformation inversion technique [7]. Both approaches will be investigated in next year's work.

The variance in the experimental data is demonstrated in Fig. 12. The outer ring (θ=60°) time domain defect impulse responses for experiment

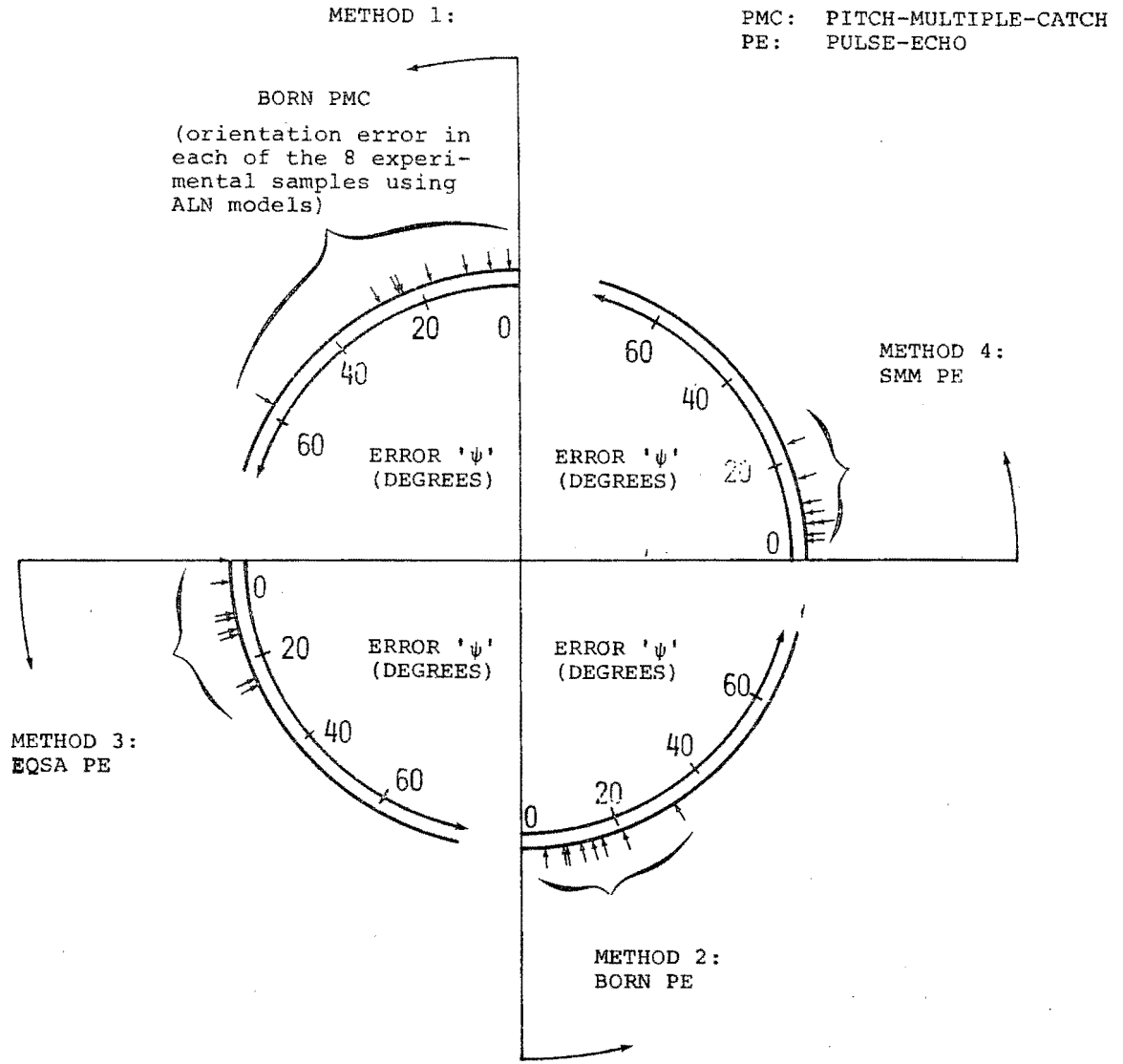
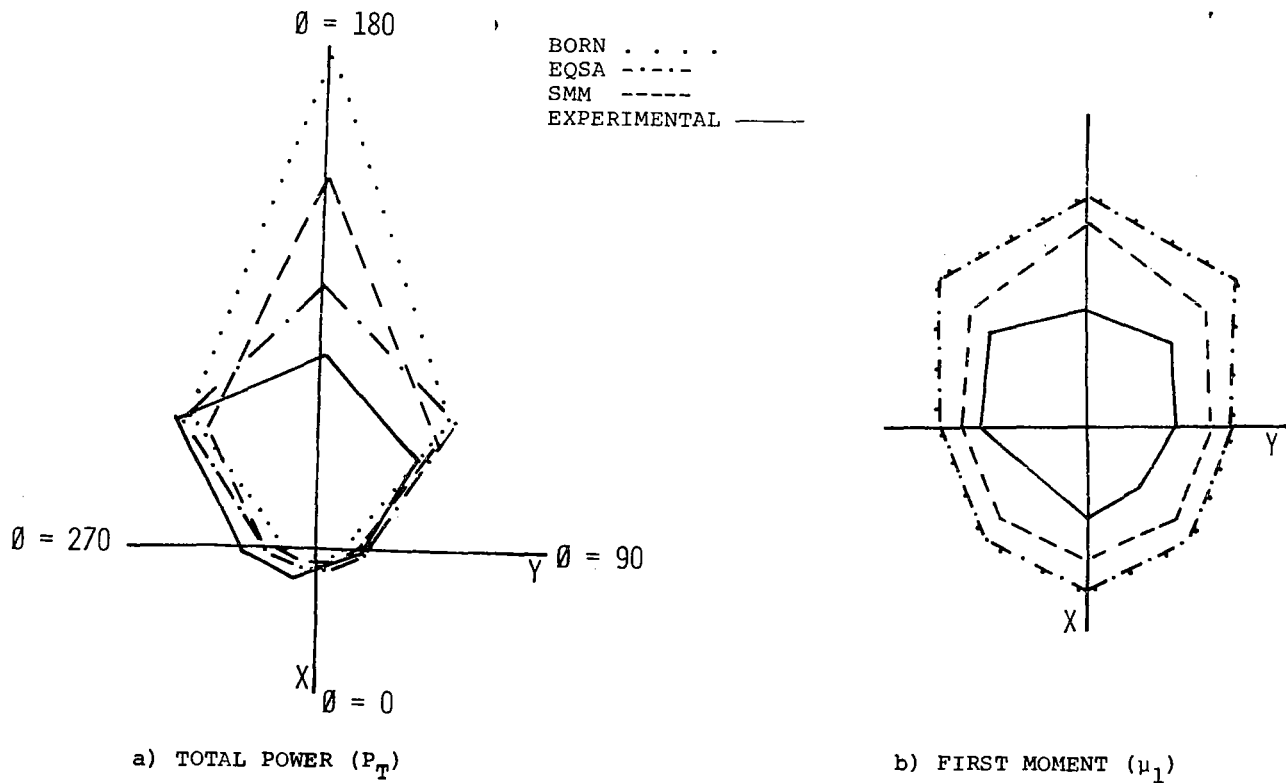


Fig. 9. Scatter plot illustrating the error between the true and estimated defect orientation. (Perfect estimation would result in no scatter about the 0° point.)

Table 4. Important features selected by the ALN models to estimate A, B, α , β .

a) BORN PMC				b) BORN PE			
Primary Feature	Receiver Group	Secondary Feature Description	Useful For Estimating	Primary Feature	Receiver Group	Secondary Feature Description	Useful For Estimating
P_T	OR	Circular variance	B, α	P_T	IR	Average value	A, B, α
P_T	OR	S-part of circular mean	B, α	P_T	IR	S-part of circular mean	A, B
P_T	OR	Circular mean	β	P_T	OR	S.D.	B, α , β
P_T	IR	Average of S.D.'s for ORT's	A	P_T	OR	Circular mean	β
P_T	IR	RI ratio for T = 0	α	μ_1	OR	C-part of circular mean	A, α
P_T	IR	RI ratio for T = 90	α	μ_2	IR	Average value	A, B
μ_1	IR	Second eigenvalue of P-matrix	A	μ_2	All	Third eigenvalue of C-matrix	A, B
μ_1	IR	S.D. of S.D.'s for ORT's	B, α	μ_2	OR	S-part of circular mean	α
μ_1	IR	Circular Variance	B, α	c) EQSA PE			
μ_1	OR	Circular Variance	B				
μ_1	OR	C-part of circular mean	B, α				
μ_1	OR	Circular mean	α				
μ_1	IR	C-part of circular mean	α				
μ_1	IR	RI ratio for T = 0	α				
μ_1	IR	RI ratio for T = 90	α				
μ_1	IR	RI ratio for T = 270	α				
μ_1	IR	S.D. of S.D.'s for ORT's	A				
μ_2	OR	Circular Variance	B, β				
μ_2	OR	Circular mean	B, α				
μ_2	OR	S-part of circular mean	B				
μ_2	IR	RI ratio for T = 90	α				
A_2	OR	Circular variance	A				
A_2	IR	RI ratio for T = 90	α				
A_2	IR	RI ratio for T = 180	α				
A_2	IR	RI ratio for T = 270	α				
d) SMM PE				Primary Feature	Receiver Group	Secondary Feature Type	Useful For Estimating
P_T	OR	Average value	α , β	P_T	IR	Average value	A, B
P_T	OR	S.D.	A, α	P_T	OR	Average value	A, B, α
P_T	IR	Circular variance	α	P_T	OR	S.D.	A, B, α
P_T	OR	C-part of circular mean	B	P_T	IR/OR	Ratio of averages	α
P_T	β -plane	Ratio of inner to outer power	α	P_T	β -plane	Average value	A, B, α , β
P_T	β -plane	First moment	α	P_T	OR	Circular variance	B, α
P_T	OR	Circular mean	β	P_T	OR	Circular mean	β
P_T	All	First eigenvalue of C-matrix	A	P_T	β -plane	Second moment	A
P_T	All	Second eigenvalue of C-matrix	A	P_T	β -plane	Ratio of inner to outer power	A
P_T	All	Third eigenvalue of C-matrix	α , β	P_T	All	First eigenvalue of C-matrix	α
μ_1	OR	Average value	B	μ_2	OR	Average Value	A, B, α , β
μ_1	All	First eigenvalue of C-matrix	A				
μ_1	All	Second eigenvalue of C-matrix	B				
μ_1	All	Third eigenvalue of C-matrix	A, B				
μ_2	OR	Average value	B				

P_T = Total power
 μ_1 = First moment
 μ_2 = Second moment
 A_2 = A_2 coefficient
 IR = Inner ring
 OR = Outer ring



DEFECT SIZE: 100 X 400 μm OBLATE SPHEROID
 DEFECT ORIENTATION: $\alpha = 30^\circ$; $\beta = 180^\circ$
 TRANSDUCERS: 8 IN INNER RING ($\theta=30$), PULSE-ECHO MODE
 FREQUENCY RANGE: 1.0-8.8 MHz.

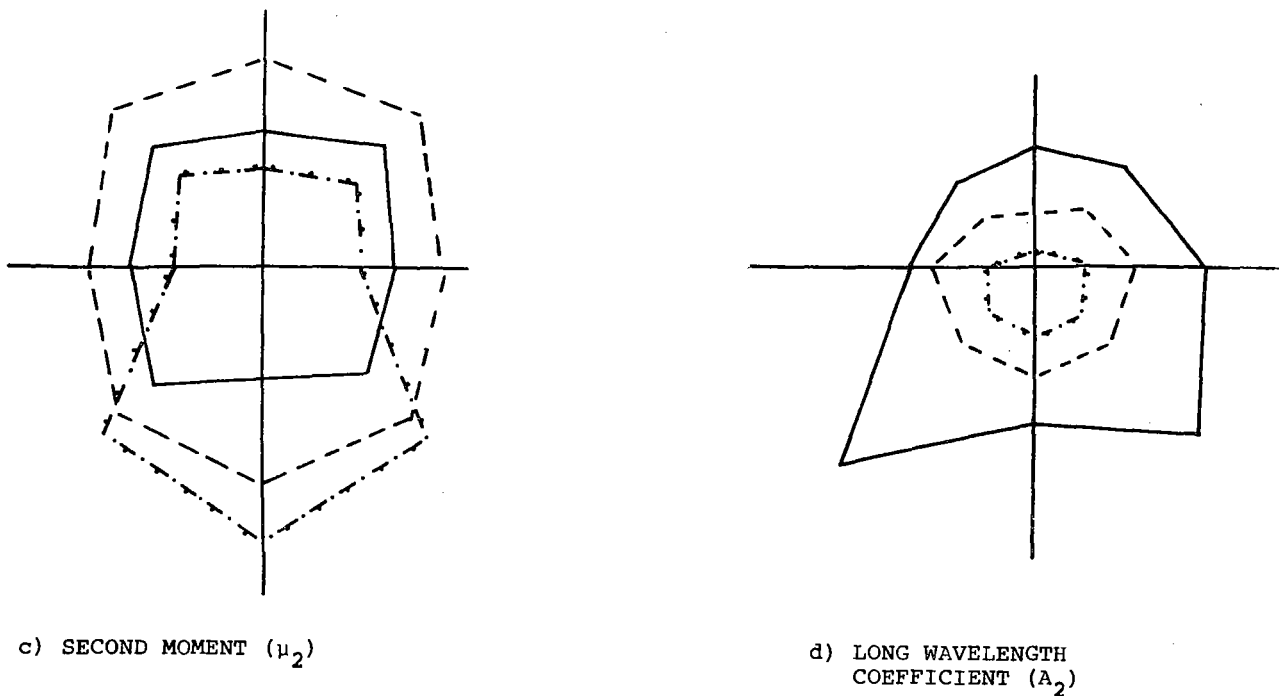


Fig. 10 Polar plots of the four primary spectral features versus azimuthal transducer position for a spheroidal void in titanium, comparing experimental data to theoretically-generated data (BORN, EQSA, SMM)

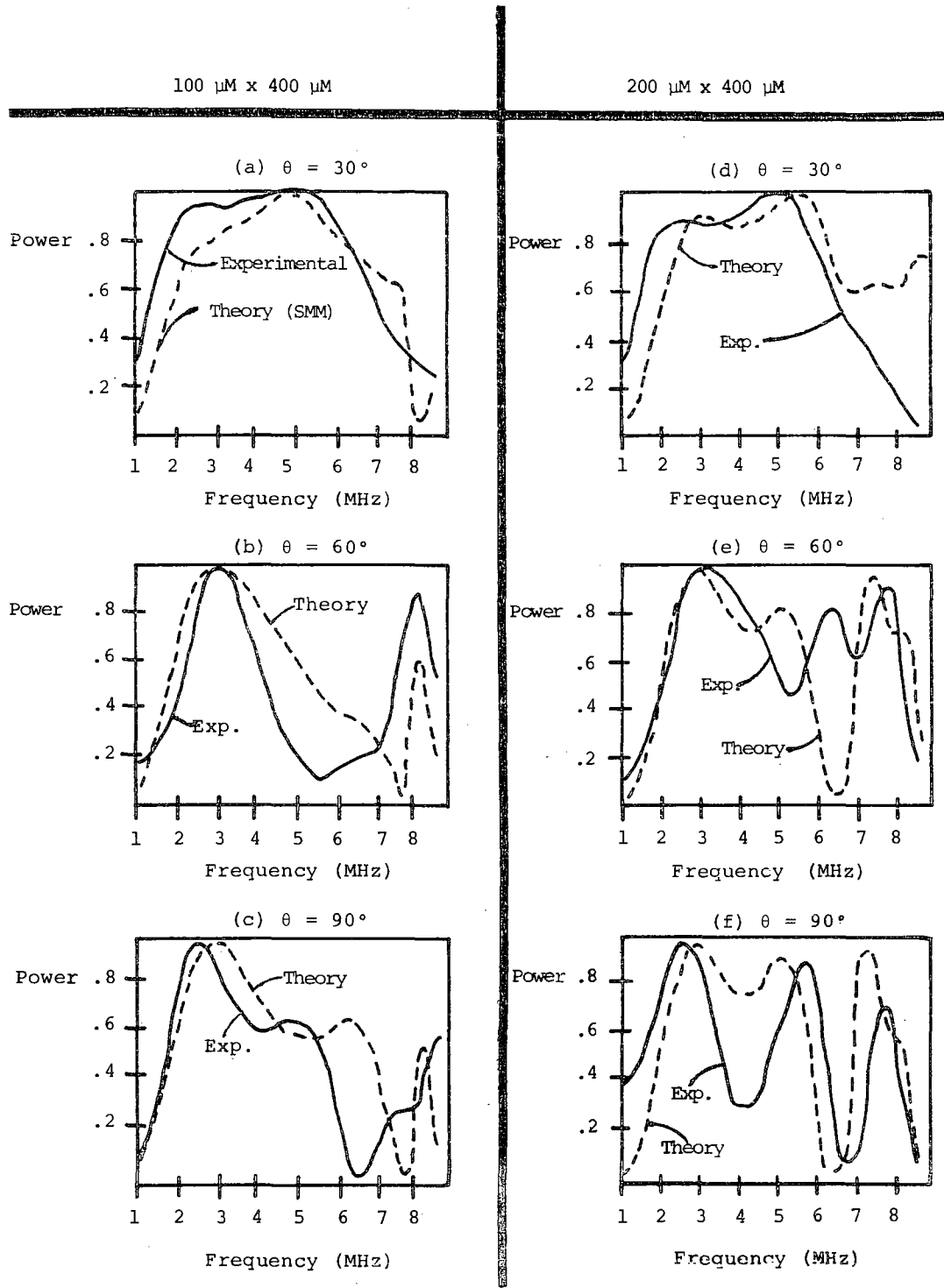


Fig. 11. Comparison of the theoretical (SMM) and experimentally obtained power spectra. Each curve was normalized by its peak value. The left three plots are for a 100 μM by 400 μM oblate spheroid at pulse-echo transducer orientations of 30, 60, and 90 degrees. The right three plots are for 200 μM by 400 μM oblate spheroid at the same PE transducer orientations.

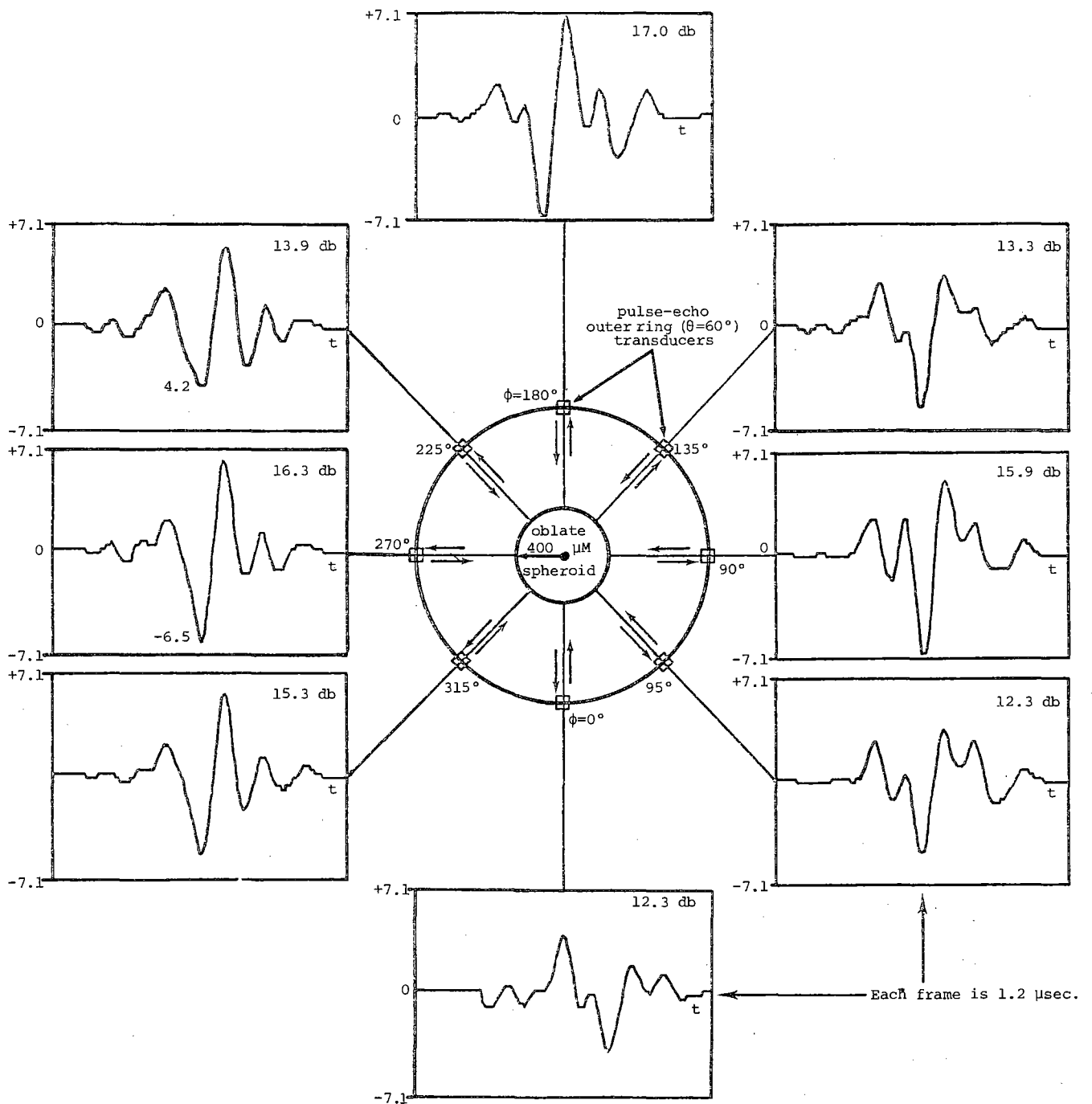


Fig. 12. Experimental pulse-echo responses from A 200 by 400 micron oblate spheroid showing the variance in the data. All experimental waveforms should be identical. The defect axis of symmetry is normal to the page. The transducers are located on the outer ring ($\theta=60^\circ$). (db values are derived from mean peak-to-peak levels)

number 1 of Table 2 are shown. This PE experiment was a 200 μM by 400 μM defect having an orientation at $\alpha = 0^\circ$ and $\beta = 0^\circ$. All outer ring transducers therefore have the same polar orientation with respect to the defect's symmetry axis. Hence, all waveforms should be identical. Note, however, that differences in peak amplitude vary up to 4.7 decibels. Also, the waveforms taken at $\phi = 0, 45,$ and 90 degrees appear to have quite different shapes than those at $\phi = 225, 270,$ and 315 degrees. Variations of this kind undoubtedly contributed to the error in the ALN size and orientation evaluations. This source of variation in the experimental data can be termed an "irreducible error" source because it provides a lower bound to the modeling error. This lower bound is not known at present but, as seen in Fig. 12, it is certainly non-zero.

DISCUSSION

The correlation coefficients ($\rho_{i,j}$) were computed between the secondary features involving A_2 , and the defect geometry parameters $A, B, \alpha,$ and β as a means of measuring the defect geometry information content of A_2 . The $\rho_{i,j}$'s were computed on the EQSA data over the 240 theoretical experiments, as:

$$\rho_{i,j} = \frac{\sum_{k=1}^{240} (x_{ik} - \bar{x}_i)(x_{jk} - \bar{x}_j)}{\sigma_i \sigma_j}$$

where the σ 's are the standard deviations of the variables. A correlation of 0.97 was found to exist between the defect's larger radius (B) and the average of the eight A_2 coefficients computed around the outer ring. The significance of this high correlation is better demonstrated in Fig. 13 where B is plotted against the average outer ring A_2 feature. All 240 experiments are represented here. Only three values of B were present in the data base, 200, 300, and 400 microns. The heavy solid lines indicate the maximum spread of the A_2 secondary features. Note that the trend is linear and the lines do not overlap.

The conclusion is that a good estimate of the defect's larger radius can be found directly from the average of several spatial estimates of A_2 . A more precise estimate could be found by combining A_2 with other features via ALN's.

A high correlation of 0.96 was found between the defect's polar angle (α) and the ratio of the average inner ring A_2 to the average outer ring A_2 . A plot of α versus this ratio feature is illustrated in Fig. 14. Again, 240 experiments were represented, and the solid lines indicate a maximum spread rather than a standard deviation. There were 10 different values of α in the data base from 1.0 to 89.0 degrees. Note the linear trend in α as the A_2 ratio increases. The spread of these ranges may be reduced greatly by considering only receivers in the β -plane.

One of the resultant ALN's is shown in Fig. 15. This model was trained with BORN-generated pulse-echo data to estimate the defect's polar angle (α). Each "element" in the network consists of a six-term quadratic multinomial of two input

variables (with the exception of element "f" which has only four terms). The input features at the left of Fig. 15 are the "secondary" spatial features computed from the scattered ultrasonic waveforms. The outputs of the leftmost elements provide inputs to subsequent elements. The rightmost element output renders an estimate for α . Nesting, or "layering", of polynomials as shown allows for many hundreds of nonlinear terms to be represented in a compact form. The ALN model structure, as well as the weighting coefficients, are developed from the empirical training data.

ACKNOWLEDGEMENT

This research was sponsored by the Center for Advanced NDE, operated by the Science Center, Rockwell International, for the Defense Advanced Research Projects and the Air Force Materials Laboratory under Contract F33615-74-C-5180.

REFERENCES

1. J. A. Krumhansl, E. Domany, J. E. Gubernatis, Rockwell International (Science Center) technical report, Interdisciplinary Program for Quantitative Flaw Definition Special Report Second Year Effort, 1975, p. 102.
2. J. E. Gubernatis, "Long Wave Scattering of Elastic Waves from Volumetric and Crack-Like Defects of Simple Shapes", Los Alamos Scientific Laboratory, Supported by USERDA.
3. V. Varatharajulu (V. V. Varadan) and Y. Pao, "Scattering Matrix for Elastic Waves .1. Theory", J. Acoust. Soc. Am., Vol. 60, No. 3, Sept. 1976.
4. J. D. Achenbach, "Applications of Geometrical Diffraction Theory to QNDE Analysis", ARPA/AFML Review of Progress in Quantitative NDE, July 17-21, 1978.
5. B. R. Tittmann, E. R. Cohen, "Experimental Measurements and Interpretation of Ultrasonic Scattering by Flaws", Interdisciplinary Program for Quantitative Flaw Definition. Special Report Third Year Effort, 1976, p. 82.
6. J. M. Richardson, "Direct and Inverse Problems Pertaining to the Scattering of Elastic Waves in the Rayleigh (Long Wave) Regime", Review of Progress in Quantitative NDE, July 17-21, 1978.
7. J. Rose, Cornell University, "Experimental and Theoretical Evaluation of Born Inversion Procedure", Review of Progress in Quantitative NDE, July 17-21, 1978.
8. R. W. Hamming, Digital Filters, Prentice-Hall, 1977, p. 45.
9. E. S. Fergeson, R. E. Twyman, V. L. Newhouse, "Deconvolution Processing for Flaw Signatures", Supported by Air Force Systems Command, Project No. F33615-75-C-5252.
10. T. J. Ulrych, T. N. Bishop, "Maximum Entropy Spectral Analysis and Autoregressive Decomposition", Review of Geophysics and Space Physics, Vol. 13, No. 1, Feb. 1975, p. 183.

DEFECT
RADIUS
"B"
(MICRONS)

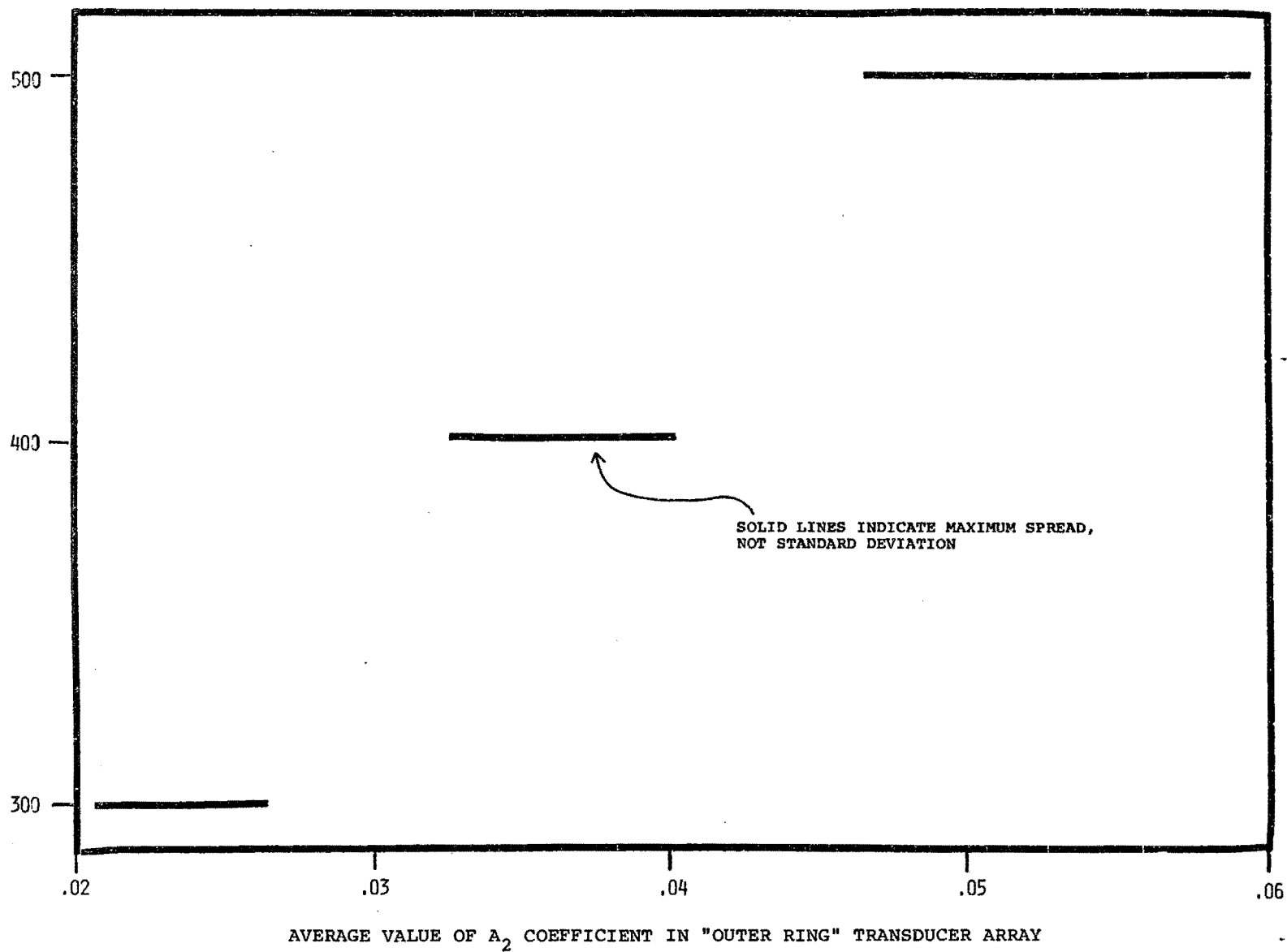


Fig. 13. Plot of defect radius "B" versus the average A_2 coefficient over 240 BORN pulse-echo experiments.

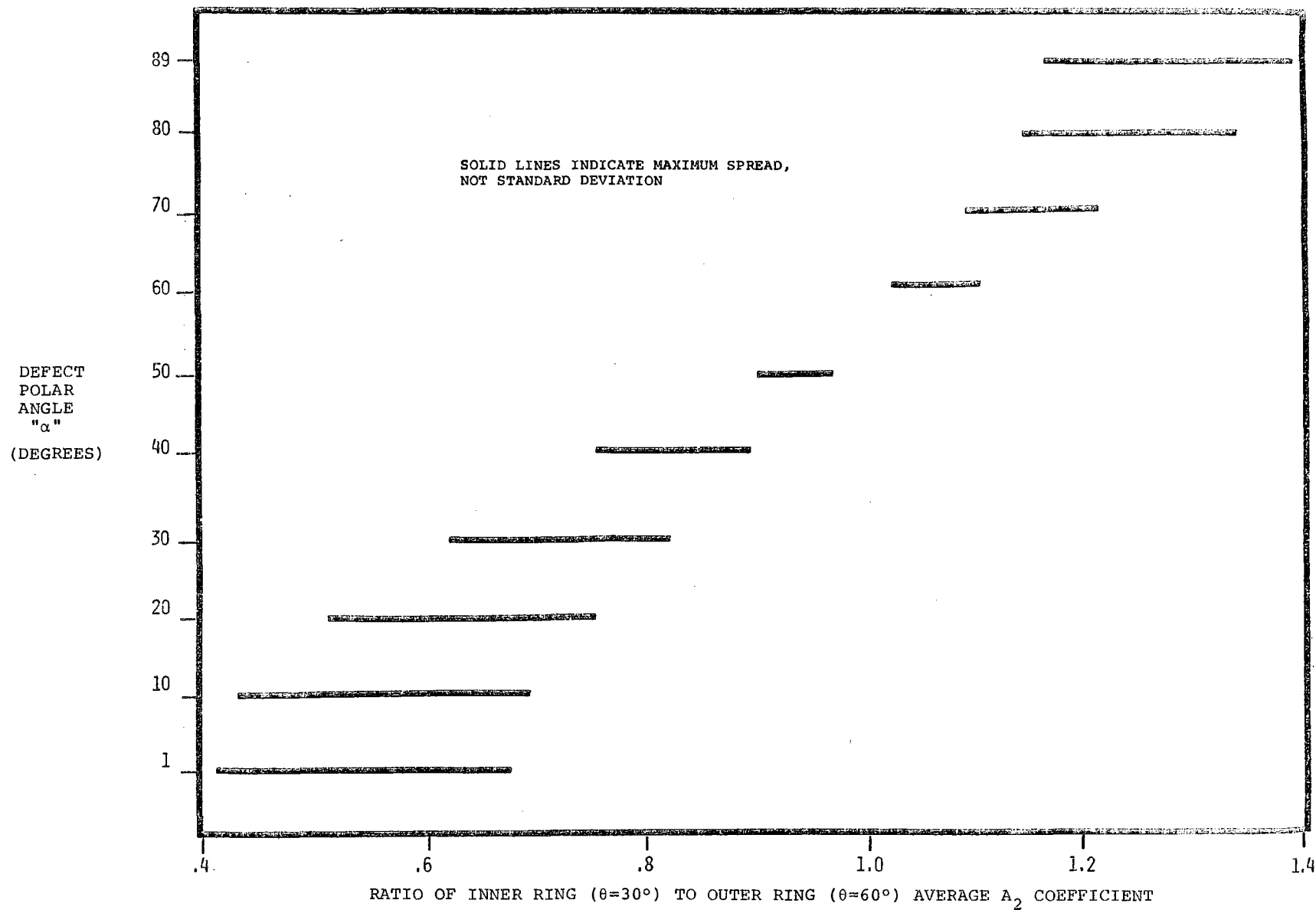
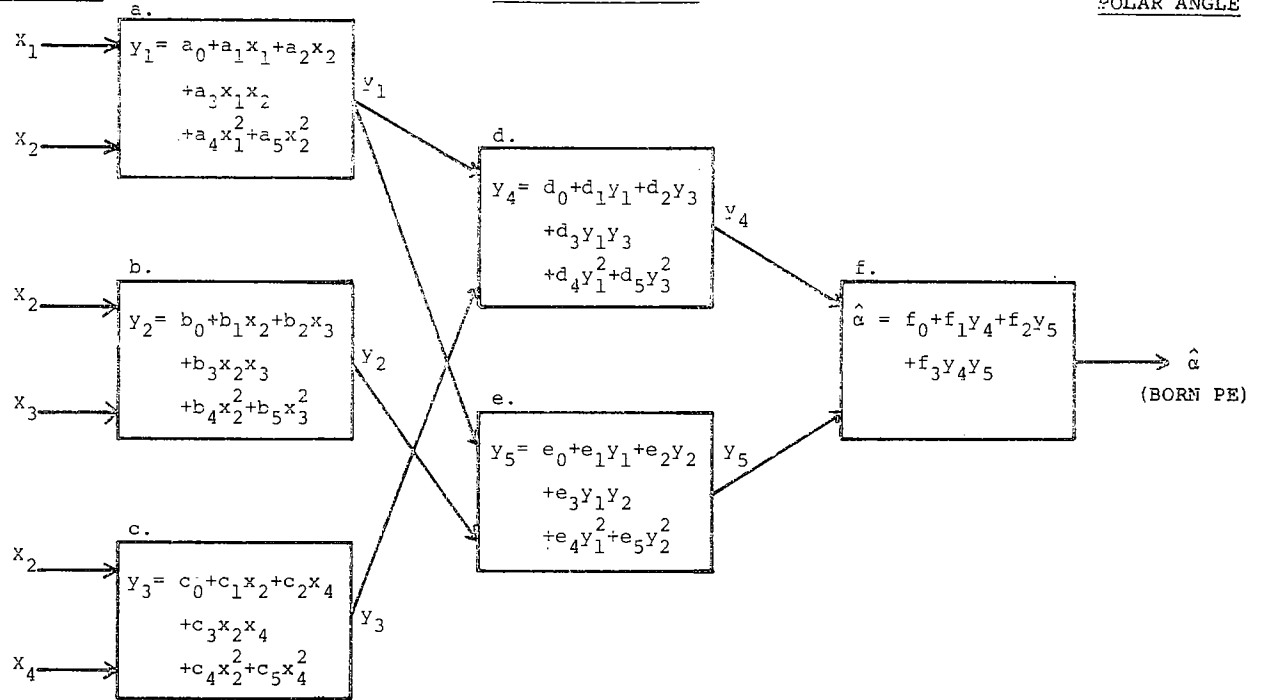


Fig. 14. Plot of defect polar angle " α " versus ratio of average A_2 coefficient from inner ring ($\theta=60^\circ$). 240 BORN pulse-echo experiments represented.

INPUT FEATURES

NETWORK ELEMENTS

ESTIMATED POLAR ANGLE



ALN WEIGHTING COEFFICIENTS

Element	0	1	2	3	4	5
a_i	.126E3	-.283E4	.375E3	.450E4	.168E5	-.230E4
b_i	.116E2	.992E3	-.577E2	.215E3	-.317E4	-.266E4
c_i	.112E2	.981E3	-.545E2	.734E3	-.329E4	-.399E3
d_i	-.178E2	.166E1	.800E0	.105E0	-.555E-1	-.656E-1
e_i	-.205E2	.103E1	.150E1	.793E-1	-.381E-1	-.581E-1
f_i	.136E0	.435E0	.482E0	.130E-2		

FEATURE DESCRIPTION

- X_1 : Average inner ring total powers
- X_2 : Standard deviation of outer ring total power
- X_3 : C-part of circular mean, outer ring first moment
- X_4 : S-part of circular mean, outer ring, second moment

Fig. 15. Adaptive Learning Network (ALN) structure for estimating the defect polar angle (α). The ALN's were synthesized using BORN-generated pulse-echo data.

11. R. W. Clayton, T. J. Ulrych, "A Restoration Method for Impulsive Functions", IEEE Transactions on Information Theory, March 1977, p. 267.
12. Mucciardi, Shankar, Whalen, "Application of Adaptive Learning Networks to NDE Methods", Interdisciplinary Program for Quantitative Flaw Definition Special Report Third Year Effort, 1976, p. 17b.
13. J. R. Rice, "Long Wavelength Defect Evaluation", Review of Progress in Quantitative NDE, July 17-21, 1978.
14. K. V. Mardia, Statistics of Directional Data, Academic Press, 1972, p. 223.

DISCUSSION

- Don Thompson (Science Center): Was there anything evident in the treatment, Mike, that would indicate a systematic preference for the pulse-echo rather than pitch-catch technique?
- M. F. Whalen (Adaptronics): The tracking of the polar angle seemed to be much better for the pulse-echo than it did for the pitch-catch. The thing that I can think of offhand is that the Born approximation is most accurate in the back scattered direction.
- Walter Kohn (Materials Research Council): Could you explain the rationale behind the polynomial expression that you use in your scheme?
- M. F. Whalen: It is basically an empirical modeling process in which we take all pair-wise combinations of the candidate features and obtain a best fit to the dependent variable that we are trying to model. In the process only the best candidates will survive. We do this first by considering all the possible candidates; the ones that have survived the first layer will be used as candidates to go into the second layer: this is extended out to as many layers as are needed until we get a sufficient fit. But there are certain means taken to avoid overfitting.
- Anthony N. Mucciardi (Adaptronics): I could further answer the question. It is a multi dimensional phase shift, if you think about it that way. Consequently, any function could be represented as a power curve. Consequently, whatever underlying unknown transfer function there may be between defect size and parameters of the wave form, can be adaptively learned. The idea is to attempt to find if the underlying function can be represented by a polynomial. You have the ability to synthesize. The reason for the choice of the two term element has to do with computational efficiency.
- Bernard Budiansky (Harvard University): In view of that explanation, why learn on theoretical models rather than the actual experimental data? Why insert a Born approximation into it?
- Anthony N. Mucciardi: It is cheaper. If you have to learn on physical data, which is what we normally do, you spend many tens of thousands of dollars developing samples, even then you can't simulate all geometries and peculiarities. If you have a model that can, at least roughly, mimic a very expensive set of samples, you can generate your sample set in the computer. To me, the value of the thing is truly powerful because in principle, you may be able to simulate very strange geometries and put defects into very peculiar places by computer to generate a theoretical set of data. With any kind of luck, you will obtain a pretty good approximation of something which may be terribly expensive or impossible to build.
- Paul Holler (Saarbrücken University): I would agree that having a forward series which fits is a very good basis for applying this empirical method to make the inversion, but I have two questions. Did you apply the minimization of the mean square or did you also apply a stockaster variation of the coefficients you get? The second question is, could you say in physical terms which variables survived in the particular cases? It is striking that with beta you only have two variables survived, in other cases up to twelve were required.
- M. F. Whalen: Each of the elements represents a least squares fit. The reason that we had only two variables that remained in the case of the beta term was simply that that was all that was needed to best solve that problem. The beta term was the easiest variable. We had two variables that did the best job and the process figured out that was all that was needed. The solutions for the size parameters were dependent on much more information. If you remember, the direction of beta can be best found by looking simply at the direction where the maximum power is directed. Nothing else is needed.